Journal of Materials Chemistry A

PAPER

View Article Online
View Journal | View Issue

Cite this: J. Mater. Chem. A, 2014, 2, 17683

Porous $ZnO/ZnCo_2O_4$ hollow spheres: synthesis, characterization, and applications in gas sensing†

Xin Zhou,[a] Wei Feng,[a] Chen Wang,[a] Xiaolong Hu,[a] Xiaowei Li,[a] Peng Sun,*[a] Kengo Shimanoe,[b] Noboru Yamazoe[b] and Geyu Lu*[a]

Received 25th August 2014
Accepted 4th September 2014

DOI: 10.1039/c4ta04386c

www.rsc.org/MaterialsA

Dispersed porous $ZnO/ZnCo_2O_4$ hollow spheres were successfully prepared by annealing the precursor, which was obtained *via* a facile one-step solvothermal method without any templates or surfactants. The X-ray powder diffraction (XRD) measurement showed that the crystal phase of the sample was a mixture of ZnO and $ZnCo_2O_4$. The field-emission scanning electron microscopy (FESEM) and transmission electron microscopy (TEM) images revealed that the as-synthesized porous $ZnO/ZnCo_2O_4$ hollow spheres had an average diameter of about 850 nm and were constructed from a large number of primary nanoparticles. To demonstrate the potential applications of such porous $ZnO/ZnCo_2O_4$ composites, the as-prepared products were used to fabricate a gas sensor that was then investigated for gas-sensing performances. Results of the test showed that this sensor had fast response kinetics to acetone at the operating temperature of 275 °C, and a high response to 100 ppm acetone, one that was about 4 times higher than that of sensors based on $ZnO/ZnCo_2O_4$ nanoparticles. The remarkable enhancement in the gas-sensing properties of the porous $ZnO/ZnCo_2O_4$ hollow spheres was attributed to their unique structure.

1. Introduction

During the past few years, research on functional materials applied in gas sensors have attracted widespread attention since they play an important role in the detection of pollutants, as well as toxic and combustible gases. Various kinds of metal oxide semiconductors have been successfully prepared and applied in gas sensors. These metal oxides have included simple metal oxides, such as α-Fe_2O_3,[1–3] SnO_2,[4–6] In_2O_3,[7,8] WO_3,[9,10] ZnO,[11,12] and NiO,[13,14] as well as mixed metal oxides, such as $ZnCo_2O_4$,[15] $ZnFe_2O_4$,[16] and $NiFe_2O_4$,[17] which are oxides of two types of transition metals with the AB_2O_4 spinel structure. Despite significant advances in the applications of these oxides, there still exist some disadvantages, such as the poor selectivity of SnO_2 and the high working temperature of ZnO (400–450 °C). Developing new sensor strategies to increase sensitivity, improve selectivity, and reduce operating temperature remains a major challenge. Intense efforts have been made to improve the performance of gas sensors, such as by doping noble metal catalysts – and, in quite feasible ways, by doping various semiconductor metal oxides.[18] Composites consisting of two or more metal oxides, such as α-Fe_2O_3/SnO_2,[19,20] ZnO/SnO_2,[21,22] SnO_2/α-Fe_2O_3,[23,24] have been successfully prepared and have indeed improved gas response.

The microstructure of the semiconductor generally affects the utility factor of the sensing body, which takes part in determining the gas response.[25] Indeed, it has been demonstrated that materials with 3 dimensions and porous structures are advantageous for obtaining high sensitivity in sensing applications. Due to well-defined interior voids, high specific surface area, low density and good surface permeability, hollow nanostructures have attracted growing interest in recent years, and, because of their wide applications, the controllable synthesis of such hollow nanostructures deserve more attention as well.[26] The general approach for preparing hollow structures has involved the controlled deposition of the designed materials (or their precursors) onto diverse templates such as colloidal particles, carbon spheres, emulsion micelles, and gas bubbles, followed by selective removal of the templates *via* chemical etching or thermal decomposition.[27] However, the disadvantages of the template-assisted method are its high cost and tedious synthetic procedure. Moreover, contamination of the template usually decreases the activity of the synthesized materials. Recently, a number of approaches based on Ostwald ripening and the Kirkendall effect have been developed to obtain various hollow structures.[28–31] Although much effort has been expended in this important field, it is still challenging to develop a facile, low-cost and scalable approach for the efficient

[a]State Key Laboratory on Integrated Optoelectronics, College of Electronic Science and Engineering, Jilin University, Changchun 130012, People's Republic of China. E-mail: spmaster2008@163.com; lugy@jlu.edu.cn; Fax: +86 431 85167808; Tel: +86 431 85167808

[b]Department of Energy and Material Sciences, Faculty of Engineering Sciences, Kyushu University, Kasuga-shi, Fukuoka 816-8580, Japan

† Electronic supplementary information (ESI) available. See DOI: 10.1039/c4ta04386c

synthesis of hollow micro-/nanostructures with unique and hierarchical structures.

Zinc oxide (ZnO) is an important multifunctional metal-oxide semiconductor with a stable hexagonal structure and wide band gap. Spinel $ZnCo_2O_4$ has the same shape as Co_3O_4, where divalent Zn ions occupy the tetrahedral sites in the cubic spinel structure and the trivalent Co ions occupy the octahedral sites in its crystal structure.[15,32] Both compounds have been widely applied in many fields such as gas sensors,[11,12,15] lithium-ion batteries,[33] drug delivery,[34] and optoelectronic devices.[35] Stimulated by the potentially wide applications, different morphologies and structures of ZnO and $ZnCo_2O_4$ have been prepared in the past decade. Recently, many investigations have demonstrated that the properties of oxide semiconductors can be significantly improved by formation of oxide composites. Therefore, various composites with hierarchical architectures have been prepared. However, these unique oxide composites were generally prepared by synthesizing one kind of material followed by the synthesis of the other kind of material, and such a 'two-step' procedure is tedious and ineffective. Ideally, one would prefer a one-step synthesis for preparing composites with a novel structure.

In the present work, a simple one-step solvothermal route combined with subsequent thermal treatment was employed for the preparation of uniform $ZnO/ZnCo_2O_4$ hollow spheres composed of a large number of nanoscale particles. Furthermore, to demonstrate the potential applications, a gas sensor based on the as-prepared porous $ZnO/ZnCo_2O_4$ hollow spheres was fabricated, and its sensing performances were investigated. The results showed that the as-obtained products exhibited good response to and recovery from acetone at the operating temperature of 275 °C.

2. Experimental section

2.1. Preparation

All of the chemical reagents used in the experiment were of analytical grade, purchased from Beijing Chemicals Co. Ltd. of China, and directly used without any further purification. In a typical process, 1 mmol of zinc nitrate hexahydrate ($Zn(NO_3)_2 \cdot 6H_2O$) and 2 mmol of cobalt nitrate hexahydrate ($Co(NO_3)_2 \cdot 6H_2O$) were completely dissolved into a 40 mL ethanol–ethylene glycol (EG) mixture (with a 1 : 4 ratio of the volumes of ethanol and EG) under continuous magnetic stirring. After several minutes of stirring, the transparent pink solution was transferred into a 40 mL Teflon-lined stainless steel autoclave that was then sealed, maintained at 180 °C for 12 h, and then allowed to cool to room temperature. The resulting pink precursor was collected by centrifugation and washed several times with deionized water and ethanol alternately, then dried in air at 80 °C for 12 h. Finally, the dried precipitates were annealed at 800 °C under air for 30 min to obtain porous $ZnO/ZnCo_2O_4$ composites.

2.2. Characterization

The X-ray powder diffraction (XRD) pattern of the as-prepared samples was performed on a Rigaku D/Max-2550V X-ray diffractometer with high-intensity Cu-Kα radiation ($\lambda = 1.54178$ Å) in the range of 20–70° (2θ) to examine the crystal structure. The surface morphology and microstructure of the products were directly observed by field-emission scanning electron microscopy (FESEM, JEOL JSM-7500F, operated at an accelerating voltage of 15 kV). Transmission electron microscopy (TEM) and high-resolution transmission electron microscopy (HRTEM) observations were carried out with a JEOL JEM-2100 microscope operated at an accelerating voltage of 200 kV. Energy-dispersive X-ray spectrometry (EDS) was applied to study the chemical compositions of the products, which was measured by the attached transmission electron microscope. Thermogravimetric (TG) analysis and differential scanning calorimetric (DSC) measurements were carried out using a NETZSCH STA 449F3 simultaneous thermogravimetric analyzer under air from 30 to 800 °C with a heating rate of 10 °C min^{-1}. The specific surface area of the $ZnO/ZnCo_2O_4$ hollow spheres was estimated by the Brunauer–Emmett–Teller (BET) equation based on the nitrogen adsorption isotherm obtained with a Micromeritics Gemini VII apparatus (Surface Area and Porosity System). The samples were degassed under vacuum at 160 °C for 6 h prior to the measurements.

2.3. Fabrication and measurement of gas sensor

For comparison, three gas sensors based on different kinds of sensing materials with various structures were fabricated: porous $ZnO/ZnCo_2O_4$ hollow spheres (denoted as "S1"), $ZnO/ZnCo_2O_4$ nanoparticles ("S2", see ESI Fig. S1a†), and a simple mixture of ZnO (see ESI Fig. S1b and S2†) and $ZnCo_2O_4$ nanoparticles (see ESI Fig. S1c and S3†) with a molar ratio of 1 : 1 ("S3"). The procedure used to fabricate the gas sensors, taking the sensor based on porous $ZnO/ZnCo_2O_4$ hollow spheres as an example, can be described as follows. An appropriate amount of the as-synthesized $ZnO/ZnCo_2O_4$ hollow spheres was mixed with deionized water in order to form a homogeneous paste. The paste was subsequently coated on an alumina tube, on which a pair of gold electrodes was installed at each end, and each electrode was connected with a pair of Pt wires. The alumina tube was about 4 mm in length, 1.2 mm in external diameter, and 0.8 mm in internal diameter. After drying in air at room temperature, the device was calcined at 400 °C for 2 h to improve its stability and the reproducibility of its measurements. Then a Ni–Cr alloy coil was inserted to the alumina tube as a heater, allowing us to control the operating temperature of the sensor by tuning the heating current (as shown in Fig. 1a). The gas-sensing properties of the samples were evaluated with a RQ-2 gas-sensing characterization system.

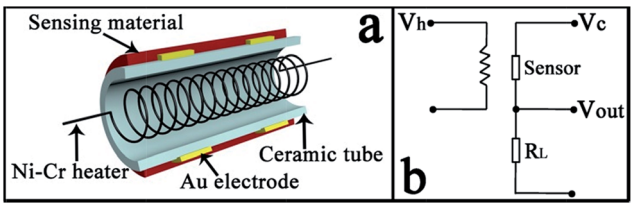

Fig. 1 Schematic diagrams of (a) the sensor and of (b) the test circuit.

The testing principle is schematically shown in Fig. 1b. The heating voltage (V_h) was supplied to the Ni–Cr alloy coil for heating the sensors, and the circuit voltage (V_c) was supplied across the sensors and the load resistor (R_L), which were connected in series. The signal voltage (V_{out}) across the load, which changed depending on the types and concentrations of the gases, was detected. The specific measurement was processed by a static process: the sensor was placed into a chamber filled with fresh air at the beginning, and then a given amount of the test gas was injected into a closed chamber by a micro-syringe. Then the sensor was put into the chamber for the measurement of the sensing performances. When the response reached a constant value, the sensor was transferred into another chamber also full of fresh air and began to recover. The gas response is defined as $S = R_a/R_g$ for reducing gas or R_g/R_a for oxidizing gas, where R_a and R_g are the resistances measured in air and the test gas atmosphere, respectively. The time it takes for the resistance to change from R_a to $R_a - 90\%(R_a - R_g)$ is defined as the response time, when the sensor is exposed to the test gas. In contrast, when the sensor is retrieved from the test gas, the time it takes for the resistance to change from R_g to $R_g + 90\%(R_a - R_g)$ is defined as the recovery time.

3. Results and discussion

3.1. Structural and morphological characteristics

Fig. 2a shows the low-magnification FESEM image of the ZnCo–glycolate precursor,[36] from which we found that the precursor was composed of a large quantity of well-dispersed microspheres with an average diameter of about 1.1 μm. Fig. 2b shows a typical high-magnification FESEM image of an individual microsphere. From a cracked microsphere depicted in Fig. 2c the inner hollow space could be clearly observed. The cluttered diffraction peaks in the XRD pattern of ZnCo–glycolate precursor shows that the precursor was amorphous (see ESI Fig. S4†). Furthermore, dispersive X-ray spectrometry was carried out to analyze the composition of the precursor, and the corresponding EDS pattern demonstrates that the as-prepared precursor consisted of the elements Zn, Co, O and C (as shown in Fig. 2d and e). Furthermore, to get insight into the possible growth mechanism of such hollow spherical structures, we surveyed the precursor morphology as a function of reaction time (when the reaction time is 1 h, no precipitate was obtained), and the results of the TEM measurements revealed that the Ostwald ripening process played an important role in the formation of the hollow spheres (see ESI Fig. S5†).[37–39]

Thermogravimetric (TG) and differential scanning calorimetric (DSC) analyses were performed to characterize the thermal properties and further determine the sintering temperature of the ZnCo–glycolate hollow spheres, which are displayed in Fig. 3. The TG curve shows that the loss of mass mainly occurred in three steps. In the early stage, the gradual loss of 2.2% of the initial weight of the ZnCo–glycolate precursor in the temperature range of 30 to 83 °C could be attributed to the removal of physically absorbed water. The following prominent 25% loss of weight between 83 and 241 °C is attributable to the thermal decomposition of ethanol and ethylene glycol molecules contained in the precursor. (The DSC curve shows a sharp exothermic peak at around 241 °C, corresponding to this dominant mass loss, which means that the transformation of amorphous precursor to $ZnO/ZnCo_2O_4$ mainly occurred at this temperature.). Finally, up to 750 °C, the slow weight loss of 3.0% could be attributed to the complete desorption of nitrate ions.

Based on the above TG and DSC analyses, we chose 800 °C as the calcination temperature for the synthesis of $ZnO/ZnCo_2O_4$ composites in order to ensure the complete decomposition of the precursor. Fig. 4 shows a representative X-ray diffraction (XRD) pattern of the product obtained by annealing the precursor at 800 °C under air for 30 min. The crystal phase of the material contained ZnO and $ZnCo_2O_4$, and most of the

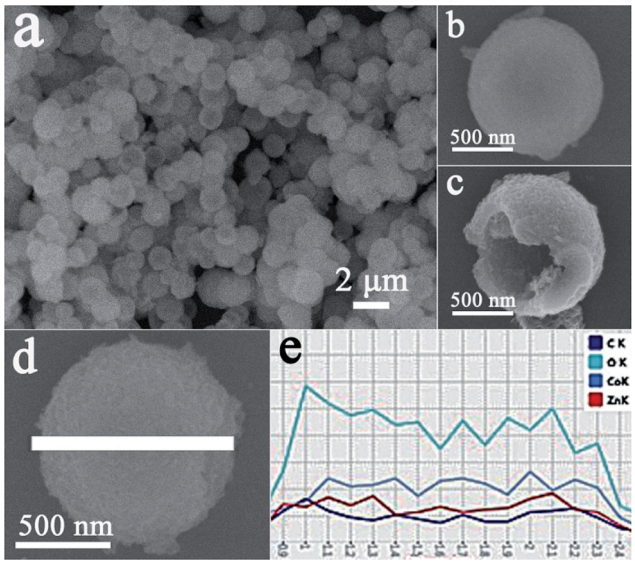

Fig. 2 (a) Low-magnification FESEM image of the precursor. (b and c) High-magnification FESEM images. (d) FESEM image of a single ZnCo–glycolate sphere, and (e) the corresponding energy dispersive spectrum (EDS) of the ZnCo–glycolate hollow sphere in (d).

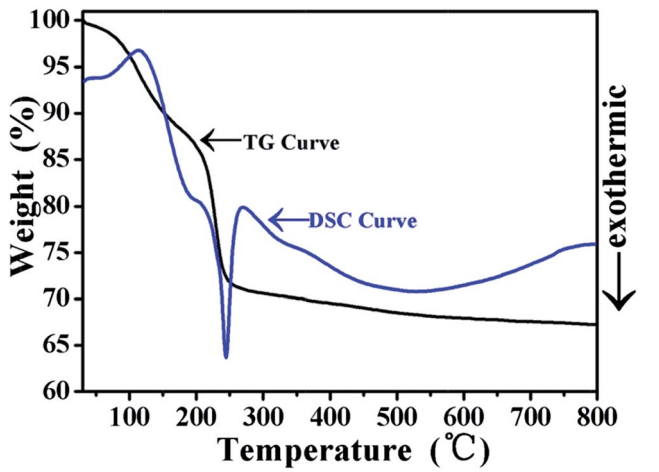

Fig. 3 TG and DSC curves of the ZnCo–glycolate precursor.

recorded diffraction peaks could be indexed to the cubic spinel structure of $ZnCo_2O_4$ with lattice constants $a = b = c = 8.095$ Å, which are in good agreement with those from the standard JCPDS card no. 23-1390. The residual peaks could be readily assigned to the hexagonal structure of ZnO, which is consistent with the standard data file no. 36-1451. The strong and sharp peaks indicate that the crystallized samples were well ordered. Furthermore, no diffraction peaks derived from any other impurities could be detected, which indicates the high purity of the sample.

Field-emission scanning electron microscopy (FESEM) and transmission electron microscopy (TEM) measurements were performed to provide detailed insight into the morphology and structure of the annealed samples (as shown in Fig. 5). A low-magnification FESEM image shown in Fig. 5a indicates that the as-prepared sample consisted of a large amount of porous spheres with an average diameter around 850 nm. The hollow spheres were observed in the high-magnification SEM image (Fig. 5b) to be composed of numerous primary particles with dimensions of tens of nanometers. Such microstructures with nanometer-sized building blocks were commonly observed in metal oxides obtained by thermal decomposition of the corresponding precursors. From a broken sphere as shown in Fig. 5c, the hollow interior could be clearly discerned. The corresponding transmission electron microscopy (TEM) images of the sample illustrated in Fig. 5d and e further clearly identify the hollow structure of the spheres, and a strong contrast between the dark edges and the pale center confirms that all of the spheres possessed a hollow cavity inside. It should be noted that the hollow sphere was observed in this image to be constructed of many nanoscaled building blocks, which is in good accordance with the observations from the FESEM images. Such a hollow and porous microstructure would facilitate the diffusion of gas molecules from the outside of the hollow microsphere into the internal space, which leads to the high utilization of the sensing body, and is therefore beneficial to gas-sensing properties.

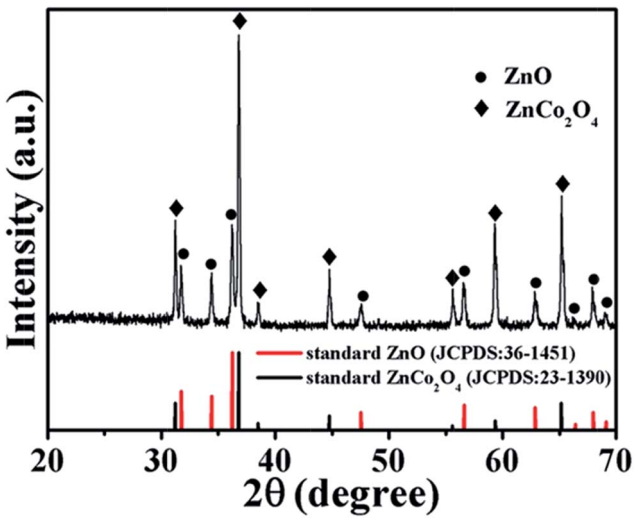

Fig. 4 XRD pattern of the porous $ZnO/ZnCo_2O_4$ hollow spheres.

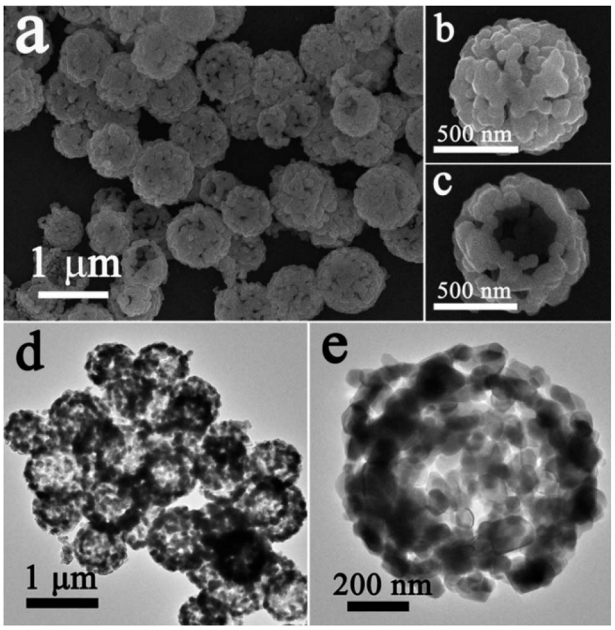

Fig. 5 (a) Typical FESEM image of porous $ZnO/ZnCo_2O_4$ hollow spheres. (b and c) High-magnification FESEM images. (d) Typical TEM image of porous $ZnO/ZnCo_2O_4$ hollow spheres. (e) High-magnification TEM image of an individual $ZnO/ZnCo_2O_4$ hollow sphere.

The high-resolution transmission electron microscopy (HRTEM) measurements and TEM elemental mapping were applied to further analyze the lattice structure and the elemental distribution of the as-prepared $ZnO/ZnCo_2O_4$ hollow structure. Fig. 6b–e shows the HRTEM images of the selected area marked with a white rectangle in Fig. 6a. The fringe spacing of 0.468 nm clearly observed in Fig. 6b and c agrees well with the spacing of the (111) lattice planes of the cubic spinel $ZnCo_2O_4$. The HRTEM images depicted in Fig. 6d and e reveal clear lattice fringes with lattice spacings of 0.281 nm and 0.260 nm, which are in good agreement with the (100) and (002) planes of the hexagonal ZnO structure. Fig. 6g shows the corresponding elemental distribution of the individual porous $ZnO/ZnCo_2O_4$ hollow sphere shown in Fig. 6f. It can be clearly seen that zinc and cobalt elements were concomitant in most regions of the sphere, but in some locations zinc could be found without cobalt (selected area marked with a white rectangle in Fig. 6g), which means that in these areas only ZnO existed. The elemental maps of Zn and Co (Fig. 6h and i) show the difference in the distributions of Zn and Co elements. Therefore, based on the analysis of the TEM elemental mapping results, it can be concluded that ZnO and $ZnCo_2O_4$ were nested within each other, forming a whole spherical shell rather than isolated ZnO and $ZnCo_2O_4$ hollow spheres.

3.2. Gas-sensing properties

Development of gas sensors with improved performance has recently become a hot topic because of increasing concerns over environmental pollution and public safety. Hollow and porous metal oxides very much favor the diffusion of target gases due to

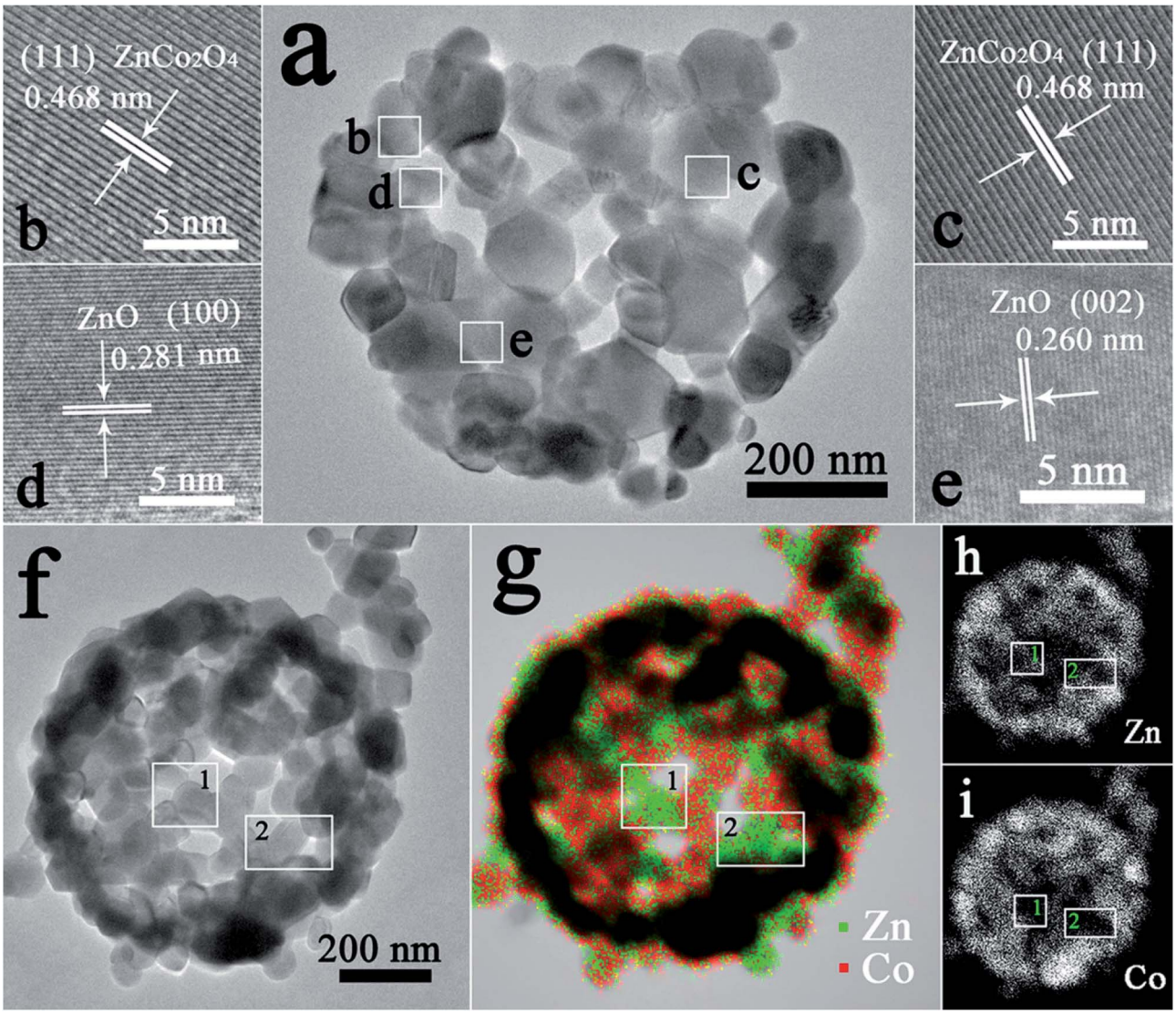

Fig. 6 (a) TEM image of a crack ZnO/$ZnCo_2O_4$ sphere. (b–e) HRTEM images recorded in different areas of (a). (f–g) TEM image of an individual porous ZnO/$ZnCo_2O_4$ hollow sphere and the corresponding elemental mapping image. (h and i) elemental maps of Zn and Co, respectively.

their well-defined pore structures.[40] Consequently, in order to verify the potential application in gas detection, gas sensors based on porous ZnO/$ZnCo_2O_4$ hollow spheres were fabricated and their gas-sensing performances were investigated. The operating temperature is important for the investigation of gas-sensing properties due to its considerable influence on the surface state of sensing materials, as well as on the reaction during the gas-sensing process.[41] Therefore, the temperature-dependence behavior of the as-fabricated gas sensor was first investigated. Fig. 7a shows the response of the three gas sensors (S1, S2, S3) to 100 ppm acetone at a series of operating temperatures from 175 to 350 °C. For the gas sensor based on hierarchical ZnO/$ZnCo_2O_4$ composites (S1), it is obvious that the response to 100 ppm acetone first increased with temperature, up to 275 °C, and then gradually decreased. The chemical interactions between the gas sensor and the test gas are known to play a significant role in the gas response of the sensor, and temperature has a great influence on the reaction; temperature thus mainly determines the gas-sensing performance. Relatively low response to gas at a low temperature is caused by the test gas molecules not having enough thermal energy to react with the surface-adsorbed oxygen species. The enhanced response with increasing the operating temperature can be attributed to two factors. One factor is that the thermal energy of the gas molecule obtained is high enough to overcome the activation energy barrier of the surface reaction; the second factor is that conversion of adsorbed oxygen species occurs by the reactions $O_{2(gas)} \rightarrow O_{2(ads)} \rightarrow O_2^-{}_{(ads)} \rightarrow 2O^-{}_{(ads)} \rightarrow O^{2-}{}_{(ads)}$, which attract more electrons from the semiconductor.[42,43] Namely, the increase of operating temperature would facilitate the chemical reaction, which leads to the increase of response to acetone. However, further increase in temperature results in the decrease of the response. The low gas adsorption ability of the gas molecule at high temperature causes the low utilization rate of the sensing material, which is the reason for the reduction in sensitivity.[26] Therefore, the change in gas response as a function

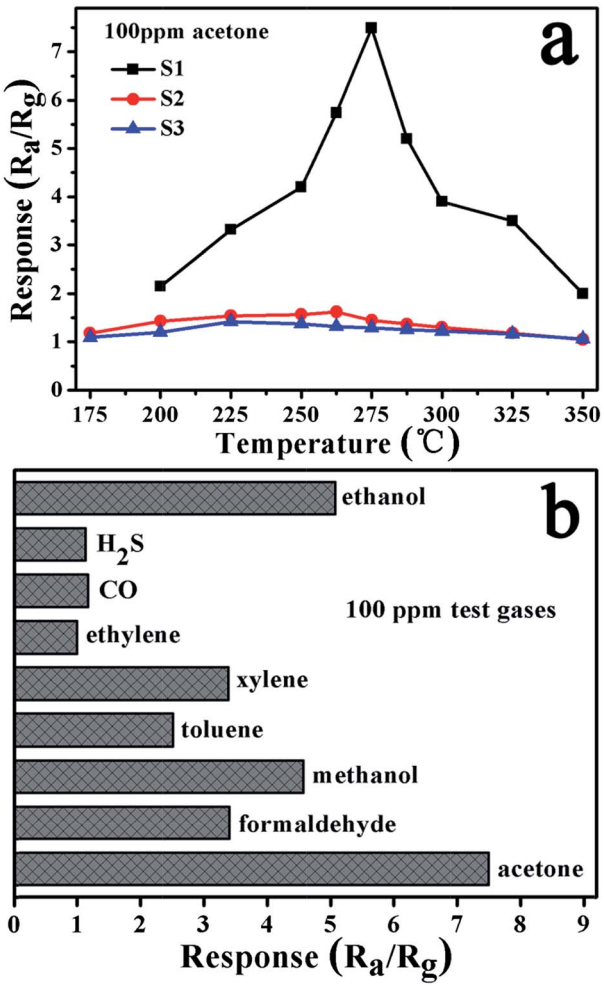

Fig. 7 (a) Responses of the as-fabricated three gas sensors (S1, S2, S3) to 100 ppm acetone as a function of the operating temperature. (b) Response of the sensor based on porous ZnO/$ZnCo_2O_4$ hollow spheres to various test gases at a concentration of 100 ppm and at an operating temperature of 275 °C.

of operating temperature shows an "increase-maximum-decay" tendency. Furthermore, it is worth noting that the response of S1 to 100 ppm acetone is about 4 times higher than that of S2 and S3. The significant enhancement in the response of S1 to acetone could be attributed to the unique porous structure of ZnO/$ZnCo_2O_4$ hollow spheres, which can dramatically facilitate diffusion of the gas.

Since selectivity is an important parameter of gas sensors for their practical application, the selectivity of the sensor based on porous ZnO/$ZnCo_2O_4$ hollow spheres was also investigated. Fig. 7b shows a bar graph of the responses of the sensor to a variety of gases, each one tested at a concentration of 100 ppm and an operating temperature of 275 °C. The response to acetone, formaldehyde, methanol, toluene, xylene, ethylene, CO, H_2S and ethanol were 7.5, 3.4, 4.4, 2.5, 3.3, 1.1, 1.2, 1.1, 5.1, respectively. Obviously, the as-fabricated sensor shows higher response to acetone than to the other gases.

The response and recovery characteristics towards different reducing gases were also investigated. Fig. 8a displays the dynamic response and recovery characteristics to 40 ppm acetone, methanol and formaldehyde at 275 °C. It is obvious that the sensor showed sensitive and reversible response to these reductive gases. Moreover, compared with methanol and formaldehyde, the sensor exhibited a much faster response to acetone. The response times to acetone, methanol and formaldehyde were 4 s, 12 s and 52 s, respectively, and the corresponding recovery times were 36 s, 31 s, 22 s, respectively. The almost square shape observed indicates that first the sensor responded rapidly to the tested gases, then the resistance of the sensor changed slowly due to analyte gases diffusing through the material and occupying the remaining surface reaction sites, and finally the resistance returned to near baseline levels when the sensor was exposed to air. Moreover, the five reversible cycles of the response–recovery curve indicates a stable and repeatable character (see ESI Fig. S6†). The dynamic response curve of the as-fabricated gas sensor to different concentrations of acetone (10–100 ppm) at 275 °C is shown in Fig. 8b. It can be seen that the response increased with the concentration of acetone. As mentioned above, the response of a sensor depends on the surface chemical reaction. Hence, for a low concentration of target gas there are fewer surface reactions occurring on the grain surface. An increase in target gas concentration

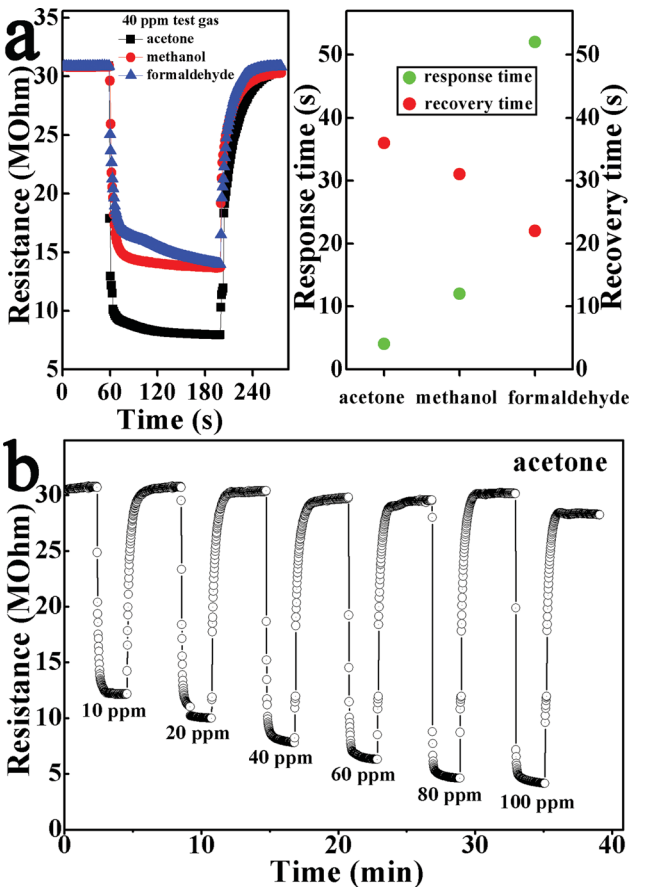

Fig. 8 (a) Response transients of the sensor using porous ZnO/$ZnCo_2O_4$ hollow spheres to 40 ppm acetone, methanol, and formaldehyde at 275 °C. (b) Response of porous hollow ZnO/$ZnCo_2O_4$ composites to different concentrations of acetone at 275 °C.

increases the number of the surface reactions and the sensitivity.[44] Therefore, the trend of increased response with increased concentration of the test gas occurred in the current experiments.

A popular and widely accepted sensing mechanism for ZnO and $ZnCo_2O_4$ is based on the change in resistance of the sensor when exposed to different types of atmospheres.[45,46] In ambient air, oxygen molecules are absorbed onto the surfaces of the $ZnO/ZnCo_2O_4$ composites and trap free electrons from the conduction band of the sensing material to form adsorbed oxygen species, including $O_2^-{}_{(ads)}$, $O^-{}_{(ads)}$ and $O^{2-}{}_{(ads)}$. As a consequence, electron depletion layers are formed on the surface of ZnO and $ZnCo_2O_4$, resulting in a reduction of the carrier concentration. When the sensor is exposed to acetone, ethanol or other reducing gases at a moderate temperature, the adsorbed oxygen species will react with these gas molecules on the material surface (eqn (1)–(3)), which leads to the release of electrons trapped in the ionized oxygen species back into the conduction band, thereby lowering the measured resistance of the sensor.[12]

$$C_3H_6O + 8O^-{}_{(ads)} \rightarrow 3CO_2 + 3H_2O + 8e^- \quad (1)$$

$$CH_3OH + 3O^-{}_{(ads)} \rightarrow CO_2 + 2H_2O + 3e^- \quad (2)$$

$$HCHO + 2O^-{}_{(ads)} \rightarrow CO_2 + H_2O + 2e^- \quad (3)$$

The working principle of gas sensors based on oxide semiconductors involves the receptor function and transducer function. In addition, the sensing performance is also determined by the utility factor of the sensing material.[25] In this case, sensor design should take fully each of three key factors into account. The good performance observed here is likely to be due to the unique architecture (hollow and porous). The porous surfaces and hollow interiors can facilitate the diffusion of the oxygen and test gases (see ESI Fig. S7†). Therefore, when the sensor fabricated by porous $ZnO/ZnCo_2O_4$ hollow spheres was exposed to test gases, not only is the resistance of the particles near the surface of the spheres affected, but the particles in the interior of spheres also become active, as illustrated in Fig. 9. In other words, the utilization rate of the sensing body is increased. This is the main reason for the high gas response in the porous $ZnO/ZnCo_2O_4$ hollow spheres.

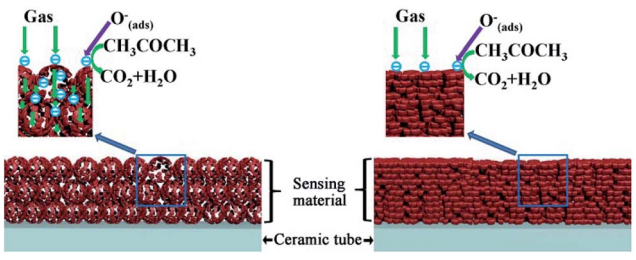

Fig. 9 Schematic diagram illustrating the possible reason for higher response of porous $ZnO/ZnCo_2O_4$ hollow spheres than that of $ZnO/ZnCo_2O_4$ nanoparticles.

4. Conclusions

In summary, a facile and controllable one-step solvothermal approach combined with a subsequent annealing process was developed for the synthesis of uniform and well-dispersed porous $ZnO/ZnCo_2O_4$ hollow spheres, which were constructed by using many primary ZnO and $ZnCo_2O_4$ nanoparticles. When such a microstructure of the $ZnO/ZnCo_2O_4$ composite was utilized as the sensing material of the gas sensor, the almost square response shape observed for acetone indicates that the sensor rapidly responded to acetone. Furthermore, there was a great enhancement in acetone sensing when compared with nanoparticles, which can be ascribed to the high porosity and unique hollow structure of $ZnO/ZnCo_2O_4$ composites. The high porosity and hollow structure of $ZnO/ZnCo_2O_4$ may also explain the ability of this composite to sense other gases as well.

Acknowledgements

This work was supported by NSFC (61134010, 61327804, 61304242, 61374218) and Program for Chang Jiang Scholars and Innovative Research Team in University (no. IRT13018), National High-Tech Research and Development Program of China (863 Program, no. 2013AA030902) and the project development plan of science and technology of Jilin Province (20130521009JH).

Notes and references

1 S. Agarwala, Z. H. Lim, E. Nicholson and G. W. Ho, *Nanoscale*, 2012, **4**, 194–205.
2 P. Sun, Z. Zhu, P. L. Zhao, X. S. Liang, Y. F. Sun, F. M. Liu and G. Y. Lu, *CrystEngComm*, 2012, **14**, 8335–8337.
3 Z. Y. Sun, H. Q. Yuan, Z. M. Liu, B. X. Han and X. R. Zhang, *Adv. Mater.*, 2005, **17**, 2993–2997.
4 S. Agarwala, W. L. Ong and G. W. Ho, *Sci. Adv. Mater.*, 2013, **5**, 1418–1426.
5 H. C. Chiu and C. S. Yeh, *J. Phys. Chem. C*, 2007, **111**, 7256–7259.
6 P. Sun, W. Zhao, Y. Cao, Y. Guan, Y. F. Sun and G. Y. Lu, *CrystEngComm*, 2011, **13**, 3718–3724.
7 T. Waitz, T. Wagner, T. Sauewasld, C. D. Kohl and M. Tiemann, *Adv. Funct. Mater.*, 2009, **19**, 653–661.
8 X. H. Sun, H. R. Hao, H. M. Ji, X. L. Lei, S. Cai and C. M. Zheng, *ACS Appl. Mater. Interfaces*, 2014, **6**, 401–409.
9 X. L. Li, T. J. Lou, X. M. Sun and Y. D. Li, *Inorg. Chem.*, 2004, **43**, 5442–5449.
10 L. Wang, A. Teleki, S. E. Pratsinis and P. I. Gouma, *Chem. Mater.*, 2008, **20**, 4795.
11 Z. H. Jing and J. H. Zhan, *Adv. Mater.*, 2008, **20**, 4547–4551.
12 D. W. Wang, S. S. Du, X. Zhou, B. Wang, J. Ma, P. Sun, Y. F. Sun and G. Y. Lu, *CrystEngComm*, 2013, **15**, 7438–7442.
13 X. F. Song, L. Gao and S. Mathur, *J. Phys. Chem. C*, 2011, **115**, 21730–21735.
14 H. Steinebach, S. Kannan, L. Rieth and F. Solzbacher, *Sens. Actuators, B*, 2010, **156**, 162–168.

15 S. Vijayanand, P. A. Joy, H. S. Potdar, D. Patil and P. Patil, *Sens. Actuators, B*, 2011, **152**, 121–129.
16 M. M. Rahman, S. B. Khan, M. Faisal, A. M. Asiri and K. A. Alamry, *Sens. Actuators, B*, 2012, **171–172**, 932–937.
17 X. F. Chu, D. L. Jiang and C. M. Zheng, *Sens. Actuators, B*, 2007, **123**, 793–797.
18 X. S. Niu, W. P. Du and W. M. Du, *Sens. Actuators, B*, 2004, **99**, 405–409.
19 P. Sun, Y. X. Cai, S. S. Du, X. M. Xiu, L. You, F. M. Liu, X. S. Liang, Y. F. Sun and G. Y. Lu, *Sens. Actuators, B*, 2013, **182**, 336–343.
20 Y. J. Chen, C. L. Zhu, L. J. Wang, P. Cao, M. S. Cao and X. L. Shi, *Nanotechnology*, 2009, **20**, 045502.
21 H. Huang, H. Gong, C. L. Chow, J. Guo,.T, J. White, M. S. Tse and O. K. Tan, *Adv. Funct. Mater.*, 2011, **21**, 2680–2686.
22 C. C. Li, X. M. Yin, Q. H. Li and T. H. Wang, *CrystEngComm*, 2011, **13**, 1557–1563.
23 D. F. Zhang, L. D. Sun, C. J. Jia, Z. G. Yan, L. P. You and C. H. Yan, *J. Am. Chem. Soc.*, 2005, **127**, 13492.
24 J. Xu, F. Huang, Y. L. Yu, A. P. Yang and Y. S. Wang, *CrystEngComm*, 2011, **13**, 4873–4877.
25 N. Yamazoe, G. Sakai and K. Shimanoe, *Catal. Surv. Asia*, 2003, **7**, 63–75.
26 P. Sun, X. Zhou, C. Wang, K. Shimanoe, G. Y. Lu and N. Yamazoe, *J. Mater. Chem. A*, 2014, **2**, 1302–1308.
27 Z. Y. Wang, L. Zhou and X. W. Lou, *Adv. Mater.*, 2012, **24**, 1903–1911.
28 B. Liu and H. C. Zeng, *Small*, 2005, **1**, 566–571.
29 Y. D. Yin, R. M. Rioux, C. K. Erdonmez, S. Hughes, G. A. Somorjai and A. P. Alivisatos, *Science*, 2004, **304**, 711–714.
30 L. Tian, X. F. Yang, P. Lu, L. D. Williams, C. H. Wang, S. Y. Ou, C. L. Liang and M. M. Wu, *Inorg. Chem.*, 2008, **47**, 5522–5524.
31 H. J. Fan, U. Gosele and M. Zacharias, *Small*, 2007, **3**, 1660–1671.
32 Y. C. Qiu, S. H. Yang, H. Deng, L. L. Jin and W. S. Li, *J. Mater. Chem.*, 2010, **20**, 4439–4444.
33 B. Liu, J. Zhang, X. F. Wang, G. Chen, D. Chen, C. W. Zhou and G. Z. Shen, *Nano Lett.*, 2012, **12**, 3005–3011.
34 H. M. Xiong, *Adv. Mater.*, 2013, **25**, 5329–5335.
35 P. D. Yang, H. Q. Yan, S. Mao, R. Russo, J. Johnson, R. Saykally, N. Morris, J. Pham, R. He and H. J. Choi, *Adv. Funct. Mater.*, 2002, **12**, 323–331.
36 L. L. Hu, B. H. Qu, C. C. Li, Y. J. Chen, L. Mei, D. N. Lei, L. B. Chen, Q. H. Li and T. H. Wang, *J. Mater. Chem. A*, 2013, **1**, 5596–5602.
37 C. Y. Christopher and H. C. Zeng, *J. Mater. Chem. A*, 2014, **2**, 4843–4851.
38 J. G. Yu, H. T. Guo, S. A. Davis and S. Mann, *Adv. Funct. Mater.*, 2006, **16**, 2035–2041.
39 H. G. Yang and H. C. Zeng, *J. Phys. Chem. B*, 2004, **108**, 3492–3495.
40 H. M. Chen, Y. Q. Zhao, M. Q. Yang, J. H. He, P. K. Chu, J. Zhang and S. H. Wu, *Anal. Chim. Acta*, 2010, **659**, 266–273.
41 X. Q. Fu, J. Y. Liu, Y. T. Wan, X. Z. Zhang, F. L. Meng and J. H. Liu, *J. Mater. Chem.*, 2012, **22**, 17782–17791.
42 G. Y. Zhang, C. S. Li, F. Y. Cheng and J. Chen, *Sens. Actuators, B*, 2007, **120**, 403–410.
43 A. M. Sutka, G. Stingaci, G. Mezinskis and J. Lusis, *Mater. Sci.*, 2012, **47**, 2856–2863.
44 A. Sutka, G. Mezinskis, A. Lusis and D. Jakovlevs, *Sens. Actuators, B*, 2012, **171–172**, 204–209.
45 X. W. Li, P. Sun, T. L. Yang, J. Zhao, Z. Y. Wang, W. N. Wang, Y. P. Liu, G. Y. Lu and Y. Du, *CrystEngComm*, 2013, **15**, 2949–2955.
46 N. Yamazoe, *Sens. Actuators, B*, 1991, **5**, 7–19.

